2019-01-1976 Published 10 Jun 2019

Surface Contamination Effects on CRM Wing Section Model

Erkki Soinne Finnish Transport and Communications Agency

Tomi Rosnell Dimensium Limited

Citation: Soinne, E. and Rosnell, T., "Surface Contamination Effects on CRM Wing Section Model," SAE Technical Paper 2019-01-1976, 2019, doi:10.4271/2019-01-1976.

Abstract

The aerodynamic effects of Cold Soaked Fuel Frost have become increasingly significant as aircraft manufacturers have applied for to allow it during aircraft take-off. The Federal Aviation Administration and the Finnish Transport Safety Agency signed a Research Agreement in aircraft icing research in 2015 and started a research co-operation in frost formation studies, computational fluid dynamics for ground de/anti-icing fluids, and de/anti-icing fluids aerodynamic characteristics. The main effort has been so far on the formation and effects of CSFF. To investigate the effects a HL-CRM wing wind tunnel model, representing the wing of a modern jet aircraft, was built including a wing tank cooling system. Real frost was generated on the wing in a wind tunnel test section and the frost thickness was measured with an Elcometer gauge. Frost surface geometry was measured with laser scanning and photogrammetry. The aerodynamic effect of the frost was studied in a simulated aircraft take-off sequence, in which the speed was accelerated to a typical rotation speed and the wing model was then rotated to an angle of attack used at initial climb. Time histories of the lift coefficient were measured with a force balance. Time histories of the upper surface boundary layer displacement thickness were measured with a boundary layer rake. For comparison the effects of typical anti-icing fluids, sandpaper and smooth PVC plastic sheet were also measured. The lift losses correlated with average surface contamination roughness height and the boundary layer displacement thickness increment.

Introduction

Cold Soaked Fuel Frost (CSFF) is formed on an aircraft wing tank area on ground when the aircraft has been at high altitude where the wing structure and fuel have been cooled down. Frost formation depends on ambient temperature, humidity and other factors such as wind speed causing forced convection. A literature review on CSFF formation is presented by Koivisto [1]. The phenomenon is known by aircraft manufacturers, airlines and the authorities, but there are only a few publications with real frost on aircraft. Ljungsröm [2] performed wind tunnel tests on NACA 65_2-A215 airfoil with abrasive paper to simulate the effect of hoar frost in representative take-off configurations with and without a flap and slat. Oolbekkink and Volkers [3] made wind tunnel tests and on NACA 63_2-015 airfoil with sandpaper as well as theoretical calculations to simulate the effect of frost. Artificial copies of real frost were made by Kind and Lawrysyn [4] and tested in wind tunnel on a flat plate to investigate the effect of frost on the boundary layer. According to Bragg et al [5] frost on an airfoil lower surface, simulated with distributed roughness particles, is significant only when it exists far enough forward to affect the upper surface boundary layer. Effects of CSFF have been studied by Koivisto in Refs. [6, 7] using a cooled wind tunnel model and real frost on two generic jet aircraft wing airfoils, the Boeing designed HL-CRM and a generic Airbus airfoil DLR-F15. Soinne and Rosnell [8] presented aerodynamic, laser scanning and photogrammetric experiments on the effects due to CSFF.

Contamination on an aircraft wing (such as ice, frost or anti-icing fluid) changes the wing surface contour but also the surface roughness. The effects of distributed roughness on multi-element airfoils was studied by Boer and van Hengst [9] using different carborundum grit to simulate frost on airfoil surface in ground icing. There was a noticeable maximum lift reduction especially with the distributed roughness also on the airfoil slat surface. Valarezo et al [10] measured the effect of inflight ice roughness on multi-element airfoils leading edge using carborundum grit and Ballottini beads. They found a noticeable effect on maximum lift reduction with ice buildup on the slat at lower take-off flap settings. Both smooth and rough in-flight ice accretion was studied in typical approach conditions by Khodadoust et al [11] on multi-element airfoils. The roughness associated with the iced surfaces was simulated by applying carborundum grit particles on top of the smooth ice shapes. The addition of roughness had a large impact on the performance degradation of the iced multi-element airfoil especially with the distributed roughness on the slat surface. However, CSFF is normally formed only on the wing tank area, not on the slat or flap.

Cold Soaked Fuel Frost is of interest for the next take-off after a turn around. Traditionally the Federal Aviation Administration of the United States has required in the

operative regulation [12] paragraph 121.629(b) that "No person may take off an aircraft when frost, ice, or snow is adhering to the wings…Takeoffs with frost under the wing in the area of fuel tanks may be authorized by the Administrator". In other words a clean wing concept has been required on the upper wing surface. The European Aviation Safety Agency has a different approach in the operative regulation [13] paragraph CAT.OP.MPA.250(b), where it says that "The commander shall only commence take-off if the aircraft is clear of any deposit that might adversely affect the performance or controllability of the aircraft". So EASA allows contamination when it does not adversely affect the operation of the aircraft. Transport Canada allows contamination on the wing in take-off in the same way as EASA, provided that there is no adverse effect. At present there is an EASA and Transport Canada approval for the Boeing 737NG aircraft to perform a take-off with a certain amount of CSFF on the wing upper surface. The FAA has also given an exemption for this aircraft.

The FAA and the Finnish Transport Safety Agency Trafi have a Research Agreement on aircraft icing research with an emphasis on ground icing such as the effects of anti-icing fluids and CSFF. The same wind tunnel model and facilities have been used on somewhat different investigations as the FAA and Trafi had overlapping interests. This research study has benefited from the expertise of Arteform Ltd, Dimensium Ltd, the FAA, NASA and Trafi.

The present investigation is focused on the wind tunnel tests of a wing model with real cold soaked fuel frost with comparisons of anti-icing and sandpaper tests. First the general background on boundary layer transition on smooth and rough airfoils as well as roughness characterization are discussed. Before the wind tunnel run the frost thickness and geometry were determined with a mechanical Elcometer gauge and using photogrammetry.

The wing model has a wing tank with surrogate fuel to cool the model for frost generation. A simulated take-off was performed by first accelerating the wind tunnel flow to simulate aircraft take-off roll on the ground and then rotating the model to an angle of attack representing initial climb. Time histories of the wing model lift coefficient and upper surface boundary layer displacement thickness were recorded during the take-off sequence. The change of the lift coefficient C_L and boundary layer displacement thickness δ^* due to contamination was determined by comparing the results with clean wing values. The effects due to contamination thickness and roughness are discussed.

Boundary Layer Transition

Smooth Airfoils

The process of transition on a clean airfoil begins with an ingestion of freestream disturbances into the boundary layer through a receptivity mechanism. The disturbances undergo an exponential growth, the dominant instability mechanism being the Tollmien-Schlichting waves for airfoils and the cross flow mode for swept wings, Matheis et al [14]. In either case a secondary instability arises, once the disturbance amplitudes have grown sufficiently, leading to a non-linear growth and production of streamwise vortices. These have an important role in redistributing the streamwise momentum vertically and lifting the spanwise vorticity from the surface resulting in a high shear layer. The high shear layer creates hairpin vortices, breaking down further downstream to smaller vortices, ultimately leading to turbulent spots. The turbulent spots grow and merge to form a fully turbulent boundary layer.

Airfoils with Distributed Roughness

The effect of surface roughness on transition depends on the roughness protrusion height in relation to the boundary layer thickness. The roughness Reynolds number is defined as

$$\mathrm{Re}_k = \frac{k u_k}{\nu} \tag{1}$$

where u_k is the velocity at the roughness protrusion height k without the roughness present, and ν is the kinematic viscosity.

The vortex structure around an isolated hemisphere on a flat plate at about Re_k=300 is shown in Figure 1. There is a primary horseshoe shaped vortex with possible secondary and tertiary vortices. On the downstream side of the hemisphere there is a separation pocket and an outflow from the pocket in the form of two spiral vortices with opposite rotation direction with respect to the horseshoe vortex. In this Reynolds number regime the flow about the disturbance element is stable and no turbulent wedge is formed downstream. The flow structure with the horseshoe vortex resembles the situation of a junction flow of a larger surface mounted streamlined body or a sharp edged cube where also a horseshoe vortex with associated flow separations is formed, see Delery [15] and Simpson [16].

When the Reynolds Re_k number is increased (Re_k=350…450) the rear separation pocket begins to become unstable. The top

FIGURE 1 Flowfield around a hemisphere formed roughness on a flat plate at Re_k=300, Ref. [18].

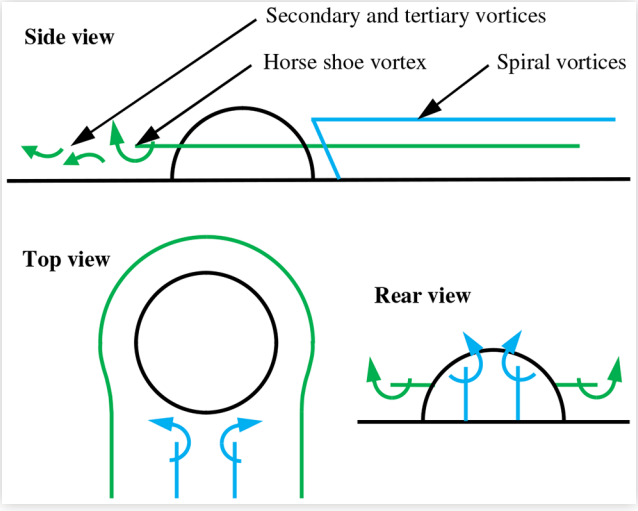

FIGURE 2 Hairpin vortices downstream of a hemisphere.

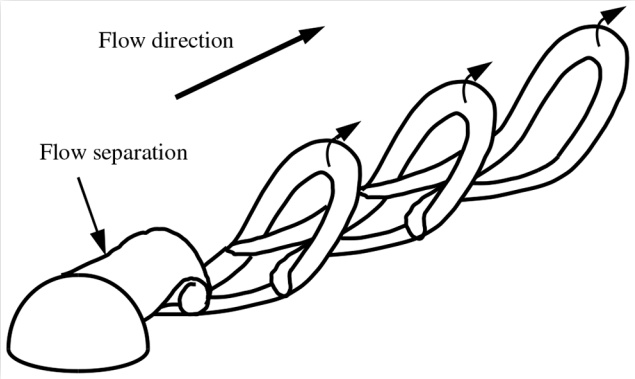

shear layer begins to shed periodic hairpin vortices, which are depicted downstream of an isolated hemisphere in Figure 2. Morkovin [17] quotes, that he has observed the formation of the horseshoe and hairpin vortices with an associated flow separation in symmetric boundary layer flows around spheres, hemispheres, cones, short cylinders, parallelopipeds and "thinner fences". There is transition downstream of the roughness element and a wedge formed turbulent area. At Re_k=600 the transition rapidly approaches the isolated roughness location. However, on a NACA 0012 airfoil leading edge an isolated three-dimensional roughness showed in measurements by Bragg et al [18] as high critical values as Re_k=1700.

When the transition and the turbulent wedge begin at the roughness element the corresponding value of Re_k is referred to as the critical roughness Reynolds number $Re_{k,crit}$. The turbulence spreads along a turbulent wedge front making an angle of roughly 10° with the streamline direction. The spreading is called transition by transverse or lateral contamination and is a bypass transition mechanism. Morkovin coined those transition types as bypass transition, which are not created through a Tollmien-Schlichting instability. An example of a turbulent wedge on a PIK-20E motor glider fuselage is shown in Figure 3. The example shows the effect of a contamination particle in a low-speed oil-flow visualization test. Despite the accelerating flow on the fuselage nose area the contamination created a turbulent wedge.

For distributed roughness of a height less than the laminar boundary layer thickness on a surface with no pressure gradient a fairly constant critical value of Re_k=600 is achieved according to Braslow et al ref. [19]. Kerho and Bragg [20] conducted wind tunnel experiments on a NACA 0012 airfoil at zero incidence with a strip close to the leading edge of constant height hemispheres with staggered but constant spacing. They found that distributed roughness generally triggered the transition process, but the resulting transitional boundary layer did not immediately reach a fully developed turbulent state. At least a length of 30% chord was required to reach that state. Matheis et al [14] performed a 3D DNS calculation on the lower Reynolds number case (Re=750000) of the same distributed roughness case. The vortex structure was complex, with vortices from a hemisphere row interacting with the vortices from the downstream row. The vortex pattern was regular and one can imagine that vortices and disturbances in a certain pattern are amplified. It has been speculated by Bragg et al [18] that the regions of dead

FIGURE 3 Turbulent wedge on PIK-20E motor glider fuselage nose in low speed oil-flow visualization tests.

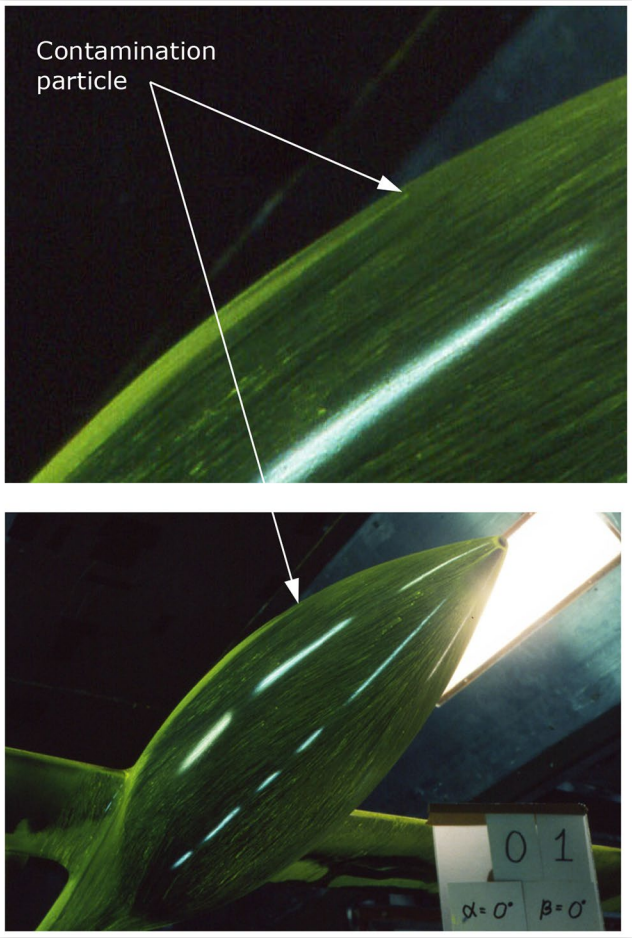

fluid in the free space between the roughness elements have low inertia and are highly susceptible to free-stream and pressure disturbances. However, it is stated by Bragg et al and Matheis et al that for distributed roughness the transition mechanism is not nearly as well understood as for the isolated case.

Cold Soaked Fuel Frost differs from stylized distributed roughness fields. It may cover the entire wing tank area. CSFF does not have a regular pattern, but the unstructured pattern may vary quite much. The frost crystals look like sharp edged bluff bodies immersed into the flow, as shown in the example of Figure 4. One can expect local flow separation, as on the isolated disturbance shapes mentioned by Morkovin. Flow separation from the highest frost peaks would lead to a formation of turbulent wedges and a successive transition to turbulent flow as shown in Figure 5.

Frost Roughness Characterization

A frost formation process is divided into a crystal growth period and a frost growth period according to Yun et al ref. [21]. Their experiments were conducted in a test channel in

FIGURE 4 Example of frost surface roughness.

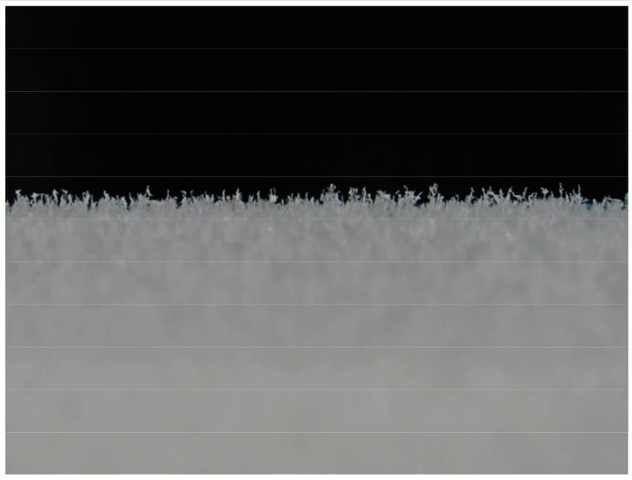

FIGURE 5 Turbulent transition wedges on a wing with Cold Soaked Fuel Frost.

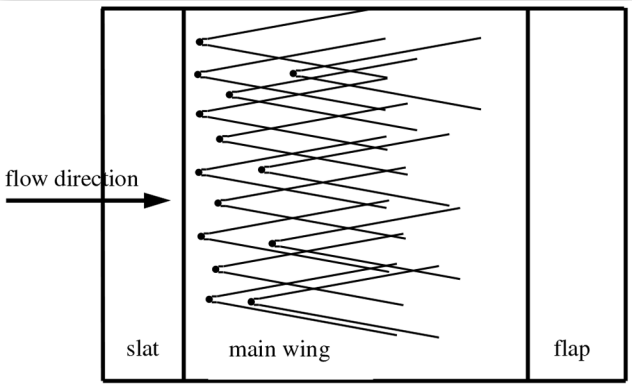

constant subfreezing temperatures, i.e. no cold soaked fuel and no radiation to space. Based on the observations in the present tests the formation of Cold Soaked Fuel Frost also contains a crystal growth period and a frost growth period. As a result there will be a solid frost layer on the surface with protrusions on top of it, see Figure 6. Surface roughness height k is the difference of the maximum and minimum thicknesses. The average frost thickness is taken as the mean value of the maximum and minimum thicknesses. Frost roughness k is understood in a similar way as sand grain roughness as frost roughness corresponds to the sand grain size. Frost roughness can be characterized with different parameters such as the height of the protrusions or the root mean square value of those. The rms value is defined in the case of n roughness height values as

$$k_{rms} = \sqrt{\frac{1}{n}\left(k_1^2 + k_2^2 + \ldots + k_n^2\right)} \quad (2)$$

FIGURE 6 Stylized roughness profile.

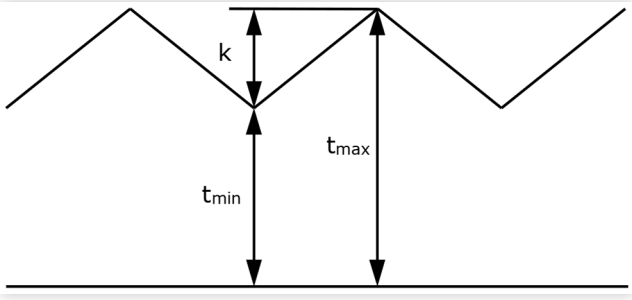

Aerodynamic Test Setup

Wind Tunnel

Arteform Low Speed Wind Tunnel is a closed circuit wind tunnel with an octagonal test section with dimensions of 2 m x 2 m and a test section length of 4 m. The flow uniformity in the test section is better than 0.14 %, and turbulence level is less than 0.28 % at a constant wind tunnel speed of 60 m/s. However, during an acceleration the turbulence level is somewhat higher, around 0.35 %. The turbulence level is relevant when a clean airfoil reference test is made. When the airfoil is contaminated (with frost or anti-icing fluid) it is not too sensitive for the tunnel turbulence level as the boundary layer is already much disturbed by the contamination.

The massive concrete structures of the wind tunnel ducts are outside the facility building. This makes the tunnel structure during winter time an efficient heat sink and the fan power, dissipated during a short period take-off run simulation, does not increase the test section temperature significantly (< 2 ° C). Temperatures in the test section follow roughly the daily outside air temperature (OAT).

HL-CRM Wing Model

CRM is an acronym for Common Research Model of a modern jet aircraft configuration. The generic long range twin engine configuration was first optimized for cruise flight and then high lift devices were added on the wing defining a HL-CRM configuration, see Lacy and Sclafani [22].

A representative section for the present studies was selected outboard of the wing planform kink as shown in Figure 7. The section was selected in the vicinity of the wing Mean Aerodynamic Chord and is free from the local flow conditions due to the engine and wing kink. In a wind tunnel test the critical flow conditions should be reproduced. Anti-icing fluid is applied on the wing upper surface only and also the possible frost on the wing upper surface is critical due to the upper surface retarding flow at high angle of attack. For this reason the section was taken in the local upper surface stream line direction. On a wing at subsonic speeds the local streamlines are directed inboard on the upper surface and outboard on the lower surface. CFD calculations by Lacy and Sclafani [22] showed that in take-off configuration at high

FIGURE 7 Wing section selection in the High-Lift Common Research Model.

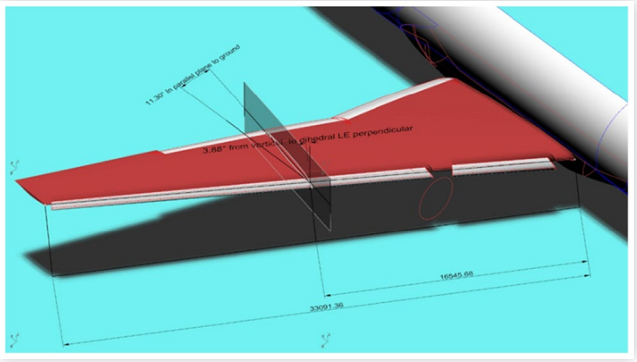

angle of attack the streamlines on the wing upper surface at the station for the representative wing section were directed 11.3° inboard. The wing section was taken in this direction and perpendicular to the wing plane to take into account the wing dihedral. In a low speed case even on a swept wing the flow speed and section perpendicular to the leading edge is not relevant, contrary to the situation in a high-speed subsonic case.

For the rectangular wing model a chord of 625 mm and span of 1550 mm were chosen as a compromise of Reynolds number, test section blockage (wind tunnel corrections) and tunnel balance forces. In the tests the slat deflection was 22° and the flap deflection 10° to give realistic take-off conditions. The test section geometry is shown in Figure 8 and named HL-CRM Mod because the section was not taken in a wing station parallel to the aircraft symmetry plane. The HL-CRM configuration external surface was not modified.

To improve the flow two-dimensionality end plates were designed for the model. Oil-flow studies at high angle of attack (Figure 9) showed a typical horseshoe vortex starting at the wing/end plate junction leading edge and confirmed attached flow at the wing upper surface and end plate corner at high angle of attack. There was a stream tube passing through the hole in the end plate and filling the corner at the vicinity of the flap leading edge. In the tunnel test section the flow is constrained by the test section walls, floor and ceiling and the wing model lift curve slope in the linear lift range was 6,103 per radian indicating a flow close to two-dimensional.

FIGURE 8 HL-CRM Mod wing model section with a slat deflection of 22o and flap deflection of 10o.

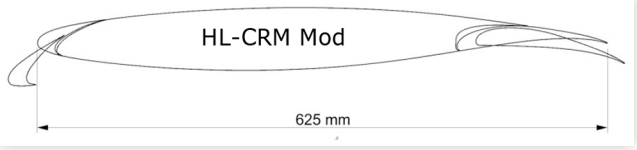

FIGURE 9 Oil-flow visualization of the wing model upper surface at α=9o and Re=1.3*10^6.

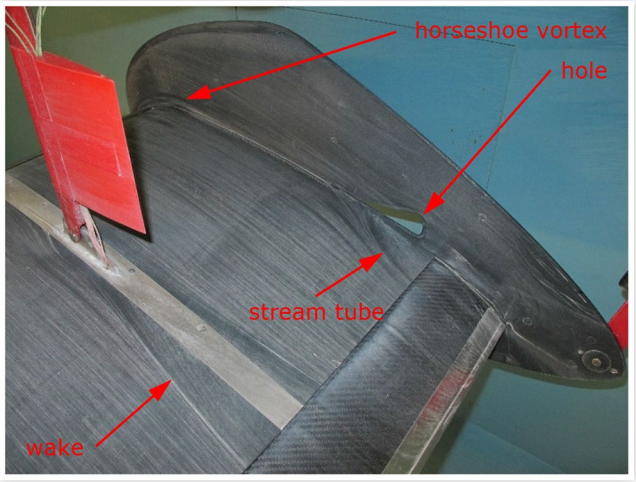

Frost Generation

The wing model coolant tank, which simulates an airliner fuel tank, is positioned between the dimensionless chord coordinates of x/c = 12% and 65%. A mixture of 50/50 ethylene glycol and water was used to simulate the effect of cold fuel. The tank was cooled down using a cooling circuit including heat exchangers inside the tank as shown in Figure 10. The cooling fluid was distributed to the heat exchangers via concentric tubes at the front and rear spars to enable a spanwise even temperature. The wing model temperature was monitored via several thermocouples inside the coolant tank and on the wing skins. The cooling system was able to reach he desired wing tank temperature of -15° C to -20° C in two to three hours. The wind tunnel test section temperature was not controlled but was the same as the ambient temperature. During the winter and spring test temperatures around zero degrees Celsius were available representing airline winter operations. The created frost thickness was measured with an Elcometer thickness gauge at several points in the tank area on the upper surface of the wing. During the wind tunnel run the cooling circuit was cut off not to disturb the force balance measurements.

FIGURE 10 HL-CRM Mod wing model with end plates.

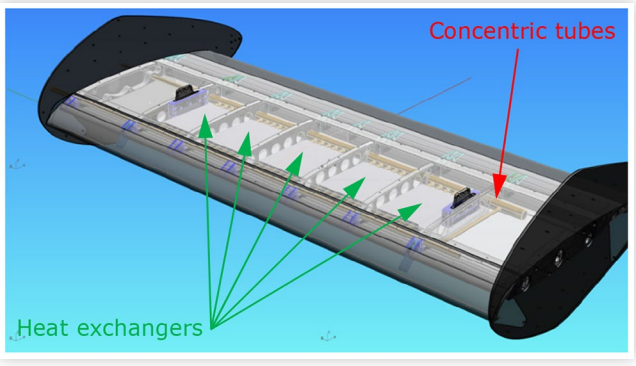

Photogrammetric Test Methodology

Camera System

Photogrammetry was performed in two campaigns in 2017 and 2018. In the first campaign there was a provisional camera system as described by Soinne and Rosnell [8]. Due to the provisional setup the photogrammetry operation took about half an hour to one hour. The resolution in point position measurements was assessed as 0.05 mm.

In the 2018 campaign an improved automatic camera system was used. The system consisted of two Nikon D850 camera bodies with Sigma ART 50mm f 1.4 lenses. The cameras were mounted to a solid camera rig supported by two sturdy camera tripods, see Figure 11. The camera rig and the cameras were operated by NMX Motion Controller and Nikon SnapBridge mobile applications. Share light model C-300RS led-type studio light was used to illuminate the object of interest.

The distance between the cameras and the wing was approximately 47cm and the distance between the sandpaper object and the cameras was approximately 44cm. Figure 12 illustrates the imaging configuration and camera rig movement between different imaging positions in frost measurements. During the wing imaging process the camera rig was moved through 30 different positions. After every 10 positions the rig was rotated 90 degrees around the vertical axis. Thus, three different image lines were captured. The imaging process took less than one minute.

FIGURE 11 Automatic camera system in the wind tunnel test section.

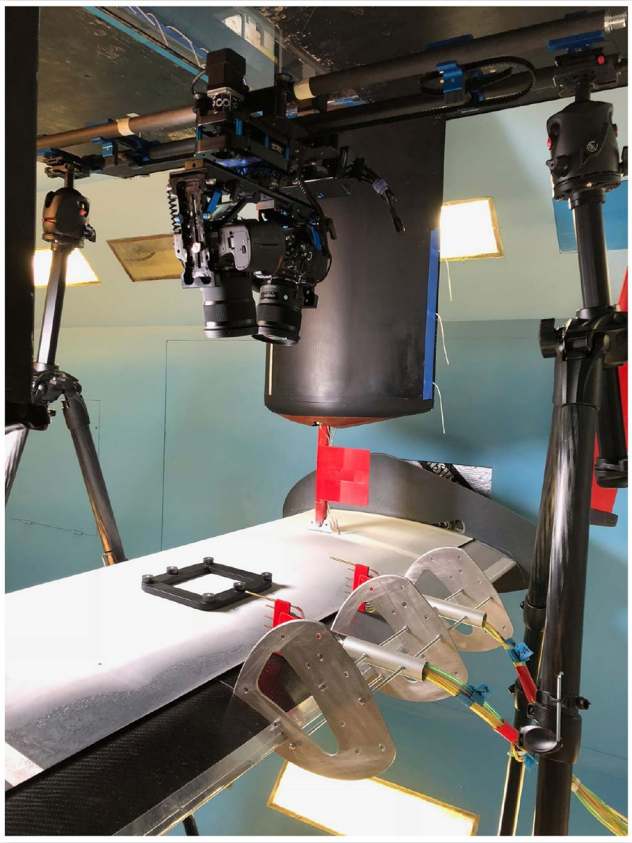

FIGURE 12 Wing imaging configuration; green dots illustrate the camera locations.

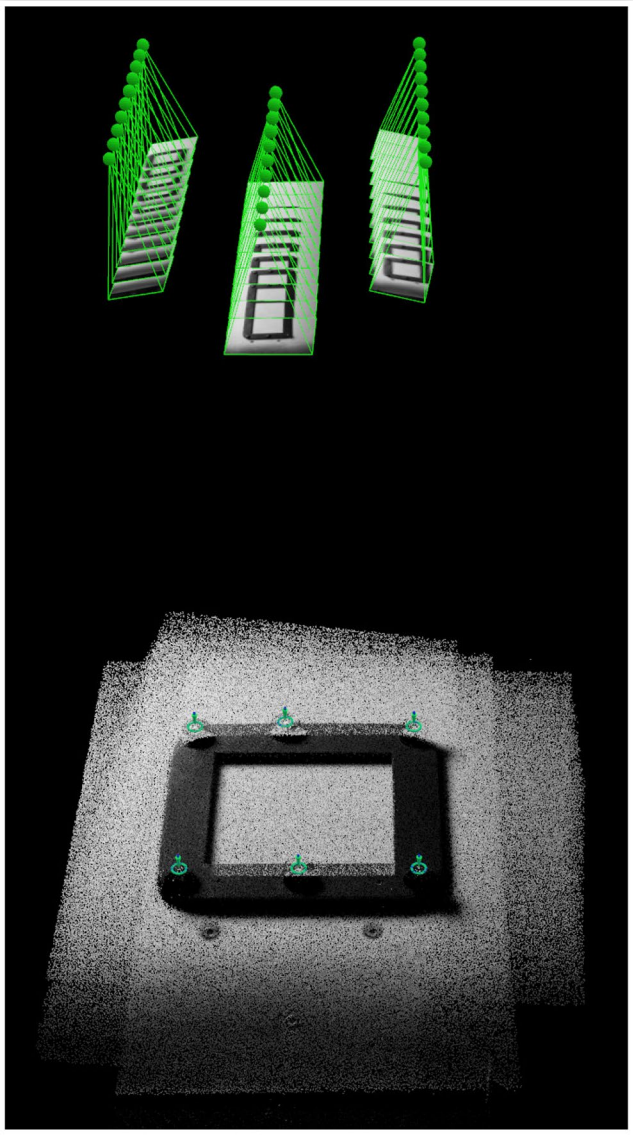

All inner camera calibration parameters were solved during the bundle block adjustment. Individual cameras of the stereo system were handled separately and combined after the individual block adjustments. Thus stereo calibration was gained for every imaging operation.

A geometrical reference object, shown in Figure 12, was used in the processing for ground support. The object contained 6 highly accurately measured targets in a metric reference system. Thus the reference object gave the right scale for the photogrammetric measurement and allowed the determination of camera self-calibration. The wing had four washers glued on top of it. These four objects were used for the point cloud alignment. The resolution in point position measurements was assessed with the automatic camera system as 0.04 mm.

FIGURE 13 Selection of t_{min} and t_{max} on the thick frost layer of February 8TH 2018.

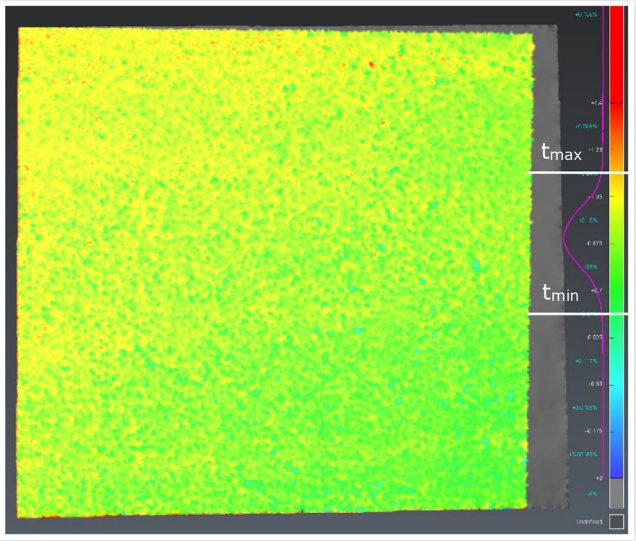

Frost Geometry Measurement

Photogrammetry produced point clouds of the frost surfaces of which an example is shown in Figure 13. A method for surface roughness estimation was developed and tested with the frost layer point clouds and with the sandpaper point clouds. With frost layer surface the roughness was evaluated by calculating a root mean square value for the frost points. The value was based on the distance between an individual point of a point cloud and a reference surface. The reference surface was the clean wing surface that was fitted to a frost layer point cloud; basically the clean wing surface was transformed in the direction of the vertical Z-axis to match the mean Z-value of the frost layer. In the sandpaper case there was not a reference surface to be used. Thus, a horizontal plane was fitted to the sandpaper point cloud to match the mean z -value of the sandpaper grain layer. The normal distances of the individual points and the plane were used to calculate the rms-value.

Frost roughness height was determined from the point clouds. The frost peak and through values were selected visually from the distributions at about 97% and 3% levels of the population. These are roughly the levels where there are noticeable changes in the distribution with almost plateaus outside the limit values. The frost layer roughness height k was taken as the difference of the maximum and minimum values. The frost layer thickness t was taken as an average of the maximum and minimum values.

Aerodynamic Test Methodology

Take-Off Sequence

The wind tunnel measurement simulates and airliner take-off sequence which consists of three parts. First there is an

FIGURE 14 Variation of wind tunnel velocity U and model angle of attack α during the simulated take-off sequence.

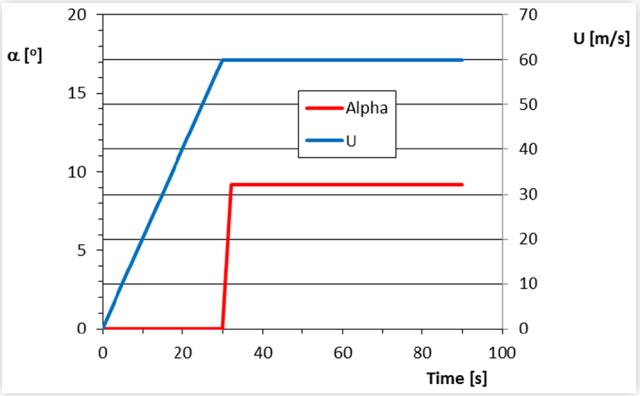

acceleration from standstill to the rotation speed V_R with a constant pitch attitude during the ground roll. Having reached the rotation speed the aircraft pitch attitude is increased to lift-off attitude. When airborne the speed is increased to take-off safety speed V_2 where it remains until the cleaning altitude. Koivisto [23] made an analysis with the Airbus performance software PEP on Airbus A321 take-off. The aircraft lift coefficient increased about ΔC_L=0.7…0.8 due to the rotation from the ground roll to initial climb angle of attack. The analysis also showed after rotation a lift coefficient peak due to the curved flight path. To simulate the peak in a wind tunnel test is too complicated a task and the test sequence in Figure 14 is a compromise. It was designed with a slat deflection 22° and flap de-flection 10°. It begins with a ground roll at zero angle of attack with a lift coefficient of about C_L=0.52. The speed increases in 30 seconds to 60 m/s and is then kept constant. When reaching the 60 m/s the angle of attack is increased to 9.2° corresponding to a lift coefficient value of about C_L=1.50. The nominal rotation rate is 4.5°/s. The wing model Reynolds number at the velocity of 60 m/s is about 2.5 million.

The purpose of the aerodynamic measurements was to correlate a certain frost thickness and roughness to a corresponding lift degradation. Another goal was to correlate the lift degradation to a corresponding boundary layer displacement thickness. Both the force balance and boundary layer rake measurements were simultaneously performed as time histories during the simulated take-off sequence. The interesting part is just after the rotation.

Measurement of Lift

The repeatability of the averaged lift coefficient values was within ±0,006. The measured balance force values contain wind tunnel corrections for flow blockage due to the model and test section boundary layer but not the effect of flow curvature. Thus the accuracy is on the repeatability of the lift coefficient, not on the absolute value. When two lift coefficient values are measured it is possible that both errors have the same sign or opposite signs resulting in an error on the difference of 0 and 0,012 respectively. Or the error on the difference

could be some value in between. Assuming that the maximum errors act simultaneously in opposite directions is probably too conservative. However, it is likely that combining two inaccurate measurements cause a larger error than in a single measurement. Often a combined error, caused by several independent factors, is estimated using a root mean square value of the individual errors. The difference of two lift coefficients will then have an inaccuracy of $\sqrt{2}$ *0,006 =0,0085.

The lift reduction due to frost was determined by estimating the average lift coefficient after the rotation with and without frost on the wing. The results are presented as a relative lift degradation $\Delta C_L/C_{LClean}$ as function of a dimensionless frost thickness t/c as a dimensionless presentation permits direct comparison with different airfoils and wings. The absolute reduction of the two-dimensional lift coefficient is transformed into a wing lift coefficient reduction in the linear range in proportion of the three and two-dimensional lift curve slopes. Consequently the absolute value of the wing lift coefficient reduction is lower than on the two-dimensional airfoil, but the relative reductions are the same. As the selected wing section for the wind tunnel model is representative for the HL-CRM jet aircraft configuration also the lift reduction is representative for the configuration.

Measurement of Displacement Thickness

The boundary layer displacement thickness values, corresponding to the lift force measurements, were measured with a boundary layer rake at the aft edge of the airfoil main element. Two different surface conditions in the same test case could be measured with two rakes simultaneously. The rake setup is shown in Figure 15. The inaccuracy of the rakes, including repeatability and the system error of the two rakes, was ± 0,44 mm on the displacement thickness increment involving two measurements as on the lift coefficient. The inaccuracy is about 6 to 32 % of the measured increments due to frost, sandpaper, anti-icing fluid and PVC plastic sheet.

The clean wing displacement thickness was about 4 mm increasing to about 12 mm for the frosted surfaces.

Results

Photogrammetry

During the wind tunnel campaigns the frost surface roughness was first measured with the Elcometer gauge and then photogrammetry. The Elcometer gauge, shown in the hand in Figure 15, is a mechanical instrument which measures if the top of the frost surface is in contact with the gauge surface. The Elcometer measurements should in principle give a thickness value close to the maximum frost thickness, but comparisons with photogrammetry results showed that the value was in most cases between the maximum and average thickness values determined by photogrammetry. It may be so, that a certain number of frost peaks are needed to be in contact with the Elcometer gauge before it is seen that a contact has been made. Another difference in Elcometer and photogrammetry is the measurement size and position. In imaging a 10 times 10 cm window was used in one representative location. The Elcometer measurements were made in 12 different point positions with an averaging of the results. Due to the wing model understructure the frost surface thickness is not exactly constant over the wing surface but has some natural variation. Both thickness measurements have advantages and drawbacks.

The frost roughness height values were derived from the photogrammetry distributions by determining the maximum and minimum thicknesses as described before. The rms values of the roughnesses were calculated for the imaged test squares using equation (2).

Lift Coefficient

An example of a time history of the model wing lift coefficient after the take-off rotation is shown in Figure 16 . Ref 1 is the

FIGURE 15 The double rake set up on the wing model and the Elcometer gauge in the hand.

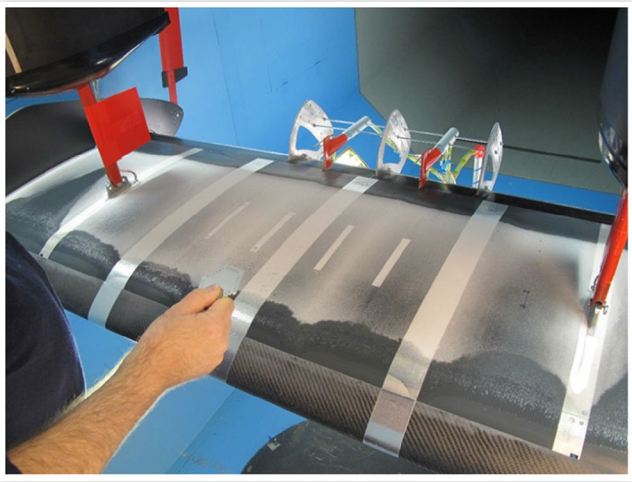

FIGURE 16 Lift coefficient time history during a simulated take-off with HL-CRM wing model.

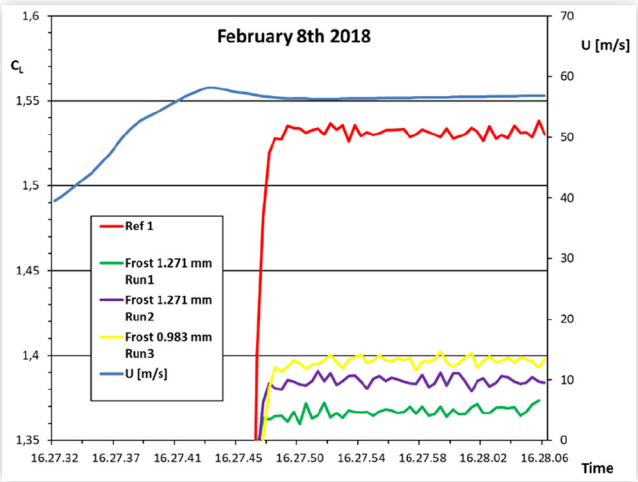

clean wing reference case and the others are successive reruns with frost. Before the first run the frost thickness was measured with the Elcometer gauge as 1.271 mm. Before the second wind tunnel run the frost thickness was not measured. The frost thickness was measured as 0,983 mm before the third run. Note that the second and third runs are performed with a frost surface which has melted/sublimated/smoothed out during and after the first wind tunnel run. One can see that already during the 20 seconds shown after the rotation of the first run the frost is somewhat reducing and the lift coefficient is slightly increasing.

The results of the two test campaigns and earlier measurements by Koivisto are summarized in Figure 17 and Figure 18. The relative lift degradation $\Delta C_L/C_{LClean}$ is presented as function of dimensionless added thickness t/c and roughness height k/c. The Elcometer gauge gives only one value for frost somewhere between the maximum and average frost thickness when the contact of the gauge is noticed by crushed frost peaks. The same value was used for both the frost thickness and roughness height. The sandpaper and PVC plastic sheet total thicknesses were measured with a micrometer. The ISO/FEPA standard average roughness value was taken as the frost roughness height. The PVC plastic sheet roughness was taken as zero. In the presentation of relative lift loss as function of the dimensionless thickness the sandpaper and PVC plastic sheet values clearly deviate from the frost results. The values fit fairly nicely in the frost results when the lift loss is presented as function of the dimensionless roughness. The rerun frost cases, indicated in the figures with a black edge, may contain inaccuracy as the frost may have melted after the first wind tunnel run. These values are slightly on the low side of the results, which may perhaps be an effect of smoothing out the frost surface. The relative degradations are only slightly different for the two airfoils at the different ambient temperatures and tend towards zero with diminishing frost thickness. There was no melting or detaching of the frost during the take-off roll noticed in the investigated cases.

FIGURE 17 Relative lift reduction as function of dimensionless thickness.

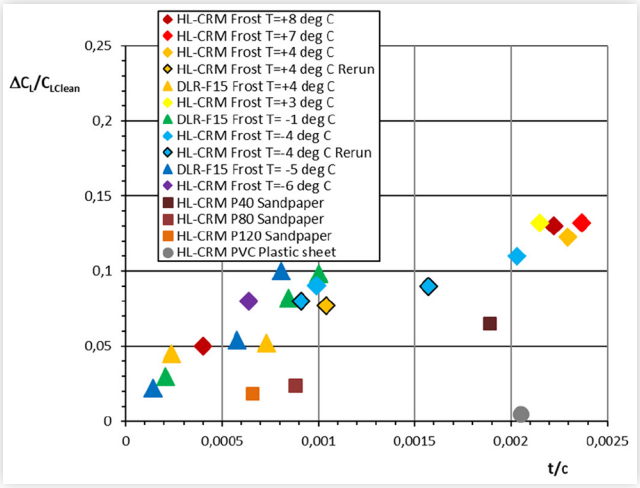

The rms value of the surface roughness, derived by photogrammetry, was a candidate for a descriptor of lift loss on distributed roughness surfaces. The wing model relative lift loss is shown in Figure 19 as function of the upper surface rms roughness divided by the model chord. The measurement point at the temperature T=-4°C with the red border contains a averaging as one half of the wing model frost surface was painted with titanium dioxide for laser scanning experiments. Photogrammetric analysis showed that there was a slight smoothing effect as the roughness height was reduced from 0.40 mm to 0.35 mm and the associated rms value changed from 0.0811 mm to 0.0635 mm. The measurement point at the temperature T=+7°C with the black border contains a slight uncertainty as a 10 cm times 10 cm test square was painted with titanium dioxide. As is seen in the figure there is no strong dependence of the lift loss on the frost rms roughness value. Also the sandpaper surfaces show a different slope. It seems that the rms roughness is not a very good descriptor of the lift loss. This can be understood with the aid of Figure 5, which shows that the upstream frost peaks are the most important in causing transition and disturbance, not all frost peaks.

FIGURE 18 Relative lift reduction as function of dimensionless roughness.

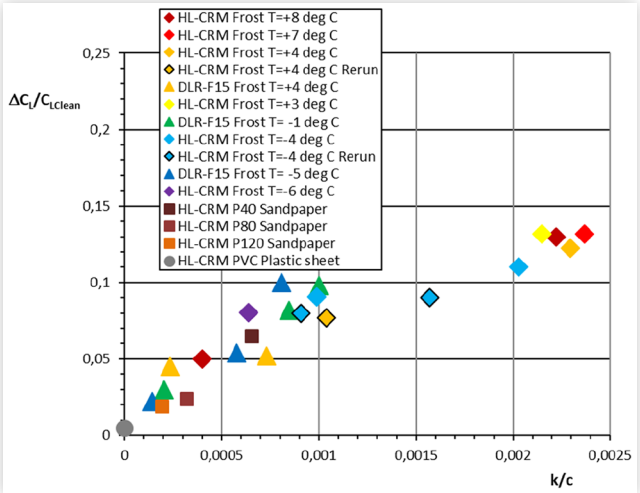

FIGURE 19 Relative lift reduction as function of surface roughness rms value divided by wing chord.

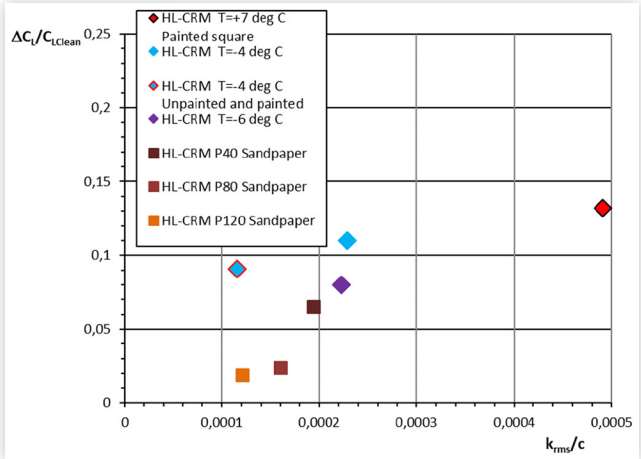

TABLE 1 HL-CRM wing section relative lift reduction values with frosted, sandpaper and PVC plastic sheet upper surface.

Case	t/c	k/c	$\Delta C_L/C_{LClean}$
Frost			
HL-CRM T=+7 deg C	0.00176	0.00208	0.132
HL-CRM T=+3 deg C	0.00212	0.00184	0.132
HL-CRM T=-4 deg C	0.00141	0.00090	0.110
HL-CRM T=-4 deg C Unpainted and painted	0.00114	0.00060	0.091
HL-CRM T=-6 deg C	0.0058	0.00091	0.080
Sandpaper			
HL-CRM P40	0.00156	0.00066	0.065
HL-CRM P80	0.00072	0.00032	0.024
HL-CRM P120	0.00056	0.00190	0.019
Plastic sheet			
HL-CRM PVC Plastic sheet	0.00205	0	0.005

Photogrammetric measurements enable the measurement of frost roughness height and average thickness as shown in Figure 13. For sandpaper the values, obtained from the ISO 3644-1 standard [24], were used. The thickness of the smooth PVC plastic layer was measured with a micrometer. The relative lift reduction is presented in Table 1 and Figure 20 as function of the dimensionless thickness and roughness. It can be seen that for the smooth layer (k/c=0) the lift reduction is very small. Consequently roughness is a more important parameter for lift reduction even if both have an effect.

Boundary Layer Displacement Thickness

The Boundary layer velocity profiles for the different frost cases at a selected time instant after the model rotation are presented in Figure 21 to give some feel for the precision needed in the measurements. One can see that the straight line profiles are somewhat angular polygons due to limiting the number of pressure tubes to eight. The calculation of the displacement thickness is transformed into determining the area of the trapeziums defining the reduced flow due to the boundary layer. Consequently the calculated displacement thickness is slightly exaggerated, but derived in the same way in each calculation.

Measurement of anti-icing fluid thickness was not possible on the wing model upper surface during a wind tunnel run, but the upper surface boundary layer displacement thickness was. Thus the wing model lift reduction could be related to the change of the displacement thickness due to the fluid or other surface roughness such as frost or sandpaper. The relative lift reduction is presented as function of the dimensionless displacement thickness change in Figure 22. The CSFF cases form a fairly linear curve of increasing relative

FIGURE 20 Iso curves of relative lift coefficient decrements $\Delta C_L/C_{LClean}$ of HL-CRM wing model as function of wing upper surface added dimensionless thickness t/c and dimensionless roughness height k/c.

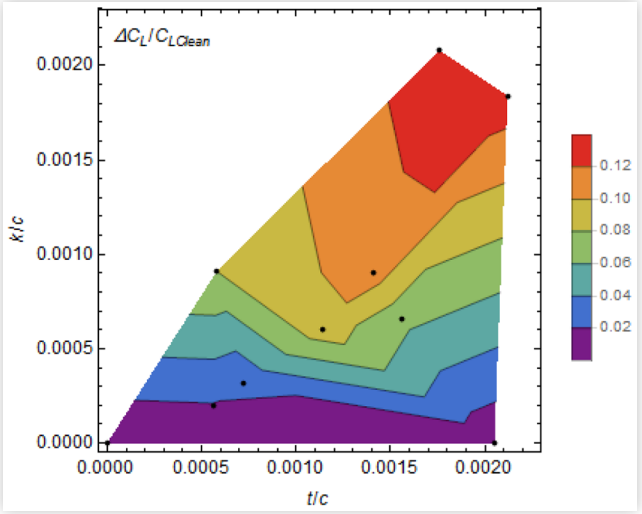

FIGURE 21 Boundary layer velocity profiles after wing model rotation.

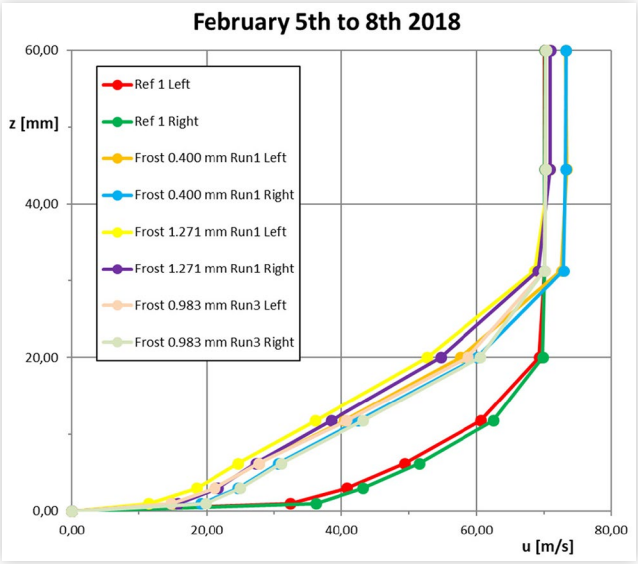

FIGURE 22 Relative lift reduction after rotation as function of dimensionless displacement thickness change.

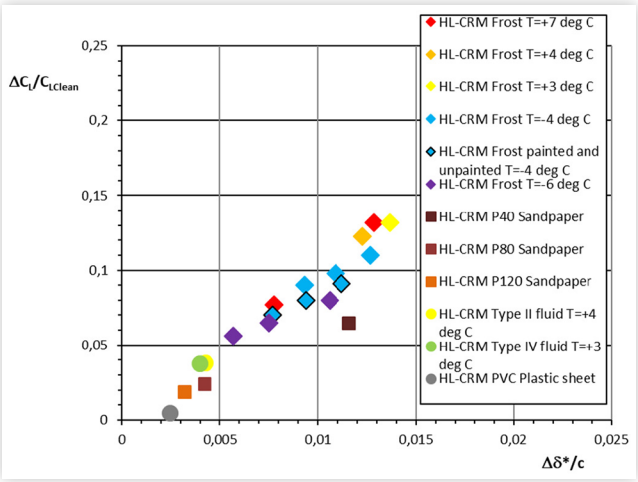

lift loss with increasing dimensionless displacement thickness change. The two examples of Type II and IV anti-icing fluids fit fairly nicely into the linear dependence curve. The sandpaper results also show linear characteristics, but with somewhat lower slope. Is it possible that the sandpaper surfaces are more regular and cause less disturbance at the same displacement thickness?

Discussion

Distributed surface contamination, such as CSFF, sandpaper and anti- icing fluid, on the upper surface of a main wing have an effect on the wing lift through the added surface thickness and roughness. A smooth additional layer has an effect due to moving the external contour and a local effect due to the forward edge of the layer. The upward movement of the section upper surface contour increases the section thickness and camber. According to classical airfoil theory a small increase in thickness and camber create in potential flow a small increase in lift. The forward edge of a layer, being of a step or ramp type, affects the viscous boundary layer and may cause an associated lift loss. A rough added layer has, besides moving the airfoil upper surface contour, also an effect through the surface roughness. The roughness disturbs the flow along the upper surface boundary layer which may cause a lift loss. Consequently a smooth added layer has one beneficial and one detrimental effect on section lift. A rough added layer has one beneficial and two detrimental effects. When wing lift experiments are performed all three effects are measured. It is however possible to separate the effects of thickness and roughness by presenting the measured lift coefficient as function of these two variables. The presented lift decrement surface showed that the dimensionless surface roughness height had a larger effect on the lift loss than the dimensionless added thickness.

Because the relative lift degradation, which is independent of the model wing aspect ratio, is a directly indicative entity it can be compared with the accepted limit values for relative lift loss due to anti-icing fluids. 5.24 % on maximum lift has been used as an acceptance limit for the anti-icing fluid effect, see Hill & Zierten Ref. [25] and Broeren & Riley Ref. [26]. The Aerodynamic Acceptance Test is however non-conservative, being based on average test results which allows half of the results to exceed the set limit. Due to the scatter in the tests results and correlations the maximum lift loss may increase from 5.24 % to the double (Soinne and Rosnell ref. [27]). There is no upper limit for the exceedance. The FAA has written a policy paper in 2015 defining an acceptable limit of 6% lift loss at liftoff, see ref. [28]. This implies a higher lift loss at maximum lift and an example of about 10 % was estimated in ref. [27].

Using the 6 % limit value Figure 18 indicates an allowable dimensionless roughness height in the order of k/c=0.0006 when the temperature is so low that there is no noticeable melting/detaching of the frost during the take-off roll. This is only an indication however, as there might be a difference in a 2D and 3D wind tunnel model lift losses. Another reason for inaccuracy in lift coefficient reduction is the Reynolds number in the present tests, which was lower than for a full scale aircraft in take-off situation. The allowable frost thickness should be confirmed with three-dimensional wind tunnel or flight testing for the aircraft configuration in question.

Summary

This paper presents lift coefficient decrements and boundary layer displacement thickness increments due to real Cold Soaked Fuel Frost and other types of distributed surface roughness. The measurements were made in wind tunnel with a surrogate fuel to cool down the wing section model. It was shown that both the frost surface thickness and roughness could be determined using photogrammetry. The dimensionless surface roughness height had a higher effect on the lift loss than the dimensionless added thickness. The boundary layer measurements enabled comparison of distributed surface roughness lift loss with anti-icing fluid effects.

References

1. Koivisto, P., "A Literature Review on Cold Soaked Fuel Frost Formation and Sublimation," Finnish Transport Safety Agency, Trafi Research Reports 6-2015, Helsinki, Finland, 2015.
2. Ljungström, B.L.G., "Windtunnel Investigation of Simulated Hoar Frost on a Two-Dimensional Wing Section with an without High Lift Devices," Report FFA-AU-902, Stockholm, Sweden, April 1972.
3. Oolbekkink, B. and Volkers, D.F., "Aerodynamic Effects of Distributed Roughness on a NACA 632-015 Airfoil," AIAA Paper 91-0443, 1991.
4. Kind, R.J. and Lawrysyn, M.A., "Aerodynamic Characteristics of Hoar Frost Roughness," *AIAA Journal* 30(7), July 1992.
5. Bragg, M.B., Heinrich, D.C., Valarezo, W.O., and McGhee, R.J., "Effect of Underwing Frost on a Transport Aircraft Airfoil at Flight Reynolds Number," *Journal of Aircraft* 31(6):1372-1379, 1994.
6. Koivisto, P., "Effects of Cold Soaked Fuel Frost on Lift Degradation during Simulated Take-off," Finnish Transport Safety Agency, Trafi Research Reports 4-2015, 2015, 24.
7. Koivisto, P., "Preliminary Cold Soaked Fuel Frost Studies with CRM Wing Model," Finnish Transport Safety Agency, Trafi Research Reports 12-2016, Helsinki, Finland, 2016, 11.
8. Soinne, E. and Rosnell, T., "Aerodynamic, Laser Scanning and Photogrammetric Measurements on Cold Soaked Fuel Frost," AIAA Paper 2018-3830, 2018, 12.
9. Boer, J.N. and van Hengst, J., "Aerodynamic Degradation Due to Distributed Roughness on High Lift Configuration," AIAA Paper 93-0028, 1993, 9.
10. Valarezo, W.O., Lynch, F.T., and McGhee, R.J., "Aerodynamic Performance Effects Due to Small Leading-Edge Ice (Roughness) on Wings and Tails," *Journal of Aircraft* 30(6):807-812, Nov.-Dec. 1993.

11. Khodadoust, A., Dominik, C., Shin, J., and Miller, D., "Effect of in-Flight Ice Accretion on the Performance of a Multi-Element Airfoil," *AHS/SAE international Icing Symposium* 10, 1995.
12. Code of Federal Regulations, Title 14 Aeronautics and Space, Volume 3, Chapter I, Subchapter G, Part 121, Federal Aviation Authority, Department of Transportation, Operating Requirements, Domestic, Flag, and Supplemental Operations, August 25, 2017.
13. Commission Regulation (EU) No 965/2012, Oct. 5, 2012, 148.
14. Matheis, B.D., Huebsch, W.W., and Rothmayer, A.P., "Separation and Unsteady Vortex Shedding from Leading Edge Surface Roughness," RTO-MP-AVT-111, 2004, 15-24.
15. Delery, J.M., "Physics of Vortical Flows," *Journal of Aircraft* 29(5), Sept.-Oct. 1992.
16. Simpson, R.L., "Juncture Flows," *Annual Review of Fluid Mechanics* 33:415-443, 2001.
17. Morkovin, M.V., "On Roughness-Induced Transition: Facts, Views and Speculations," . In: Hussaini M.V., Voigt R.G., editors. *Instability and Transition, Vol I.* (Springer-Verlag, 1990), 281-295.
18. Bragg, M., Kerho, M., and Cummings, M., Effect of Initial Ice Roughness on Airfoil Aerodynamics, AIAA Paper 94-0800, 1994, 19.
19. Braslow, A.L., Hicks, R.M., and Harris, R.V., "Use of Grit-Type Bpundary-Layer-Trnasition Trips on Wind-Tunnel Models," NASA TN-D 3579, 1966, 18.
20. Kerho, M.F. and Bragg, M.B., "Airfoil Boundary-Layer Development and Transition with Large Leading-Edge Roughness," *AIAA Journal* 35(1):75-84, Jan. 1997.
21. Yun, R., Kim, Y., and Min, M., "Modeling of Frost Growth and Frost Properties with Airflow Ovar a Flat Plate," *International Journal of Refrigeration* 25:362-371, 2002.
22. Lacy, D.S. and Sclafani, A.J., "Development of the High Lift Common Research Model (HL-CRM): A Representative High Lift Configuration for Transonic Transports," AIAA Paper 2016-0308, 24.
23. Koivisto, P., "Effects of Anti-Icing Treatment on Lift Degradation during Simulated Take-off, Finnish Transport Safety Agency," Trafi Publications 25-2013, Helsinki, Finland, 2013, 22.
24. Coated abrasives - Grain size analysis - Part 1: Grain size distribution test, International Standard ISO 6344-1, 1998-04-15, 6, 1998.
25. Hill, E.G., Zierten T.A., Aerodynamic Effects of Aircraft Ground Deicing/Anti-Icing Fluids, *Journal of Aircraft*, 30, No.1 Jan-Feb 1993, page 24-34.
26. Broeren, A.P. and Riley, J.T., "Review of the Aerodynamic Acceptance Test and Application to Anti-Icing Fluids Testing in the NRC Propulsion and Icing Wind Tunnel," NASA/TM-2012-216014, 2012, 34.
27. Soinne, E. and Rosnell, T., "Distributed Roughness Effects on CRM Wing Model, Finnish Transport Safety Agency," Trafi Research Reports 13-2018, Helsinki, Finland, 2018, 138.
28. Policy Statement, Type Cetification Policy for Approval of Use of Type II, III, and IV Deicing/Anti-icing Fluids on Airplanes Certificated Under 14 CFR Parts 23 and 25, Policy PS-ACE-23-05 PS-ANM-25-10, Federal Aviation Administration, 03/05/2015, 14.

Contact Information

The lead author email address is erkki.soinne@traficom.fi

Acknowledgments

The wind tunnel measurements were performed by Arteform Ltd. The photogrammetry measurements and post processing were performed by Dimensium Ltd. Support from the U.S. Federal Aviation Administration and Finnish Transport Safety Agency is gratefully acknowledged.

Definitions/Abbreviations

c - wing model chord
C_L - wing lift coefficient
C_{LClean} - clean wing lift coefficient
k - frost roughness height
t - frost thickness
T - temperature
U - wind tunnel velocity
V_R - rotation speed
V_2 - take-off safety speed
α - angle of attack
δ* - boundary layer displacement thickness
CSFF - Cold Soaked Fuel Frost
EASA - European Aviation Safety Agency

ISSN 0148-7191